Nanoscale

REVIEW

View Article Online
View Journal | View Issue

Graphene–nickel interfaces: a review

Cite this: *Nanoscale*, 2014, **6**, 2548

Arjun Dahal and Matthias Batzill*

Graphene on nickel is a prototypical example of an interface between graphene and a strongly interacting metal, as well as a special case of a lattice matched system. The chemical interaction between graphene and nickel is due to hybridization of the metal d-electrons with the π-orbitals of graphene. This interaction causes a smaller separation between the nickel surface and graphene (0.21 nm) than the typical van der Waals gap-distance between graphitic layers (0.33 nm). Furthermore, the physical properties of graphene are significantly altered. Main differences are the opening of a band gap in the electronic structure and a shifting of the π-band by ~2 eV below the Fermi-level. Experimental evidence suggests that the ferromagnetic nickel induces a magnetic moment in the carbon. Substrate induced geometric and electronic changes alter the phonon dispersion. As a consequence, monolayer graphene on nickel does not exhibit a Raman spectrum. In addition to reviewing these fundamental physical properties of graphene on Ni(111), we also discuss the formation and thermal stability of graphene and a surface-confined nickel-carbide. The fundamental growth mechanisms of graphene by chemical vapor deposition are also described. Different growth modes depending on the sample temperature have been identified in ultra high vacuum surface science studies. Finally, we give a brief summary for the synthesis of more complex graphene and graphitic structures using nickel as catalyst and point out some potential applications for graphene–nickel interfaces.

Received 3rd October 2013
Accepted 15th January 2014

DOI: 10.1039/c3nr05279f

www.rsc.org/nanoscale

1. Introduction: comparison of graphene interfaces with different transition metals

The interfaces between graphene and late transition metals have been thoroughly studied in recent years.[1,2] The interest in metal–graphene interfaces mainly stems from the possibility for synthesizing large area graphene films on metals by chemical vapor deposition (CVD).[3–8] In these cases the metal acts as a catalyst for complete dehydrogenation of hydrocarbon precursors that leaves carbon behind at the surface. Noble metals like Au and Ag may not exhibit high enough catalytic activities to dehydrogenate these precursors, however, even on gold CVD growth of graphene was demonstrated under appropriate conditions.[9] Other approaches for graphene synthesis on less reactive metals that do not require activation of a precursor, such as physical vapor deposition of carbon,[10,11] have also been used.

Depending on the metal and temperature during growth carbon will diffuse into the bulk. The amount of carbon in the bulk depends on the carbon solubility of the metal and this property is important to determine whether graphene grows at the surface of the metal at high growth temperatures, as it is the case for copper, or carbon dissolves into the bulk at high growth temperatures, as it is the case for nickel.[12] Materials that dissolve a larger quantity of carbon in the bulk can also precipitate more appreciable amounts of carbon to the surface upon cooling from high growth temperatures and consequently these materials, including nickel, tend to form graphitic layers (multilayers of graphene). However, the thermodynamically driven precipitation can be controlled kinetically to some extent. For example rapid cooling[13] or low temperature and low hydrocarbon exposures[14] have been employed successfully to control carbon diffusion to the surface and thus help mono- or few- layer graphene formation, even on materials with large carbon solubility. Table 1 gives a comparison of the carbon solubility in different transition metals. The high carbon

Table 1 Carbon solubilities (atom%) in different transition metals at 1000 °C according to ref. 17

Metal	Carbon solubility (atom%) at 1000 °C
Co	3.41
Ni	2.03
Cu	0.04
Ru	1.56
Rh	0.89
Pd	5.98
Ag	0.01
Re	4.39
Ir	1.35
Pt	1.76
Au	0.01

Department of Physics, University of South Florida, Tampa, FL 33620, USA. E-mail: mbatzill@usf.edu

solubility in nickel implies that the conditions for monolayer growth need to be low precursor pressures and lower temperatures. In the case of nickel the formation of graphene at low temperatures is complicated by the presence of another carbon containing surface phase. It has been known for a long time that carbon forms a surface-carbide, *i.e.* a single atomic monolayer ordered Ni_2C phase, on the Ni(111) surface.[15,16] The presence of additional carbon containing surface phases on Ni makes the formation of graphene slightly more complex than on most other transition metals and we will discuss the interplay between these carbon containing surface phases in more detail below.

The interfaces between graphene and various metals differ in two main aspects: (i) lattice mismatch, and (ii) metal–graphene interaction. In terms of lattice mismatch the Ni(111) surface is the closest matched interface with respect to graphene of all transition metals. The close lattice match enables the formation of a 1×1 structure of graphene on Ni(111) under most vacuum growth conditions, while on all the other metals a periodic lattice matching condition results in a moiré superstructure. For metals with fairly strong interaction the low index direction of graphene are usually aligned with those of the metal substrate after CVD growth.[1] This is *e.g.* the case for graphene on Ru, Rh, Re. A metal that interacts weaker with graphene but may still form an aligned surface structure under correct growth conditions is Ir(111)[5] and under some growth conditions also on Au(111)[11] and Cu(111).[18] However, for most growth conditions, graphene on Cu and on other weakly interacting metals, such as Pt, exhibits different rotational domains with respect to the metal substrates.[19]

One measure of the interaction strength between graphene and metals is the graphene–metal separation. For strongly interacting metals this separation may depend on the position within the moiré pattern. Only in locations where the graphene has the appropriate position with respect to the substrate the bonding can be optimized and the separation is minimized. For most metal surfaces the adsorption configuration is with one carbon atom located at a metal atop site and the other carbon atom in a three-fold hollow site of a hexagonal metal substrate layer. In Fig. 1 the different low symmetry adsorption configuration of a hexagonal graphene lattice with respect to a lattice matched metal are illustrated. In Table 2 the measured and/or computed graphene–metal separation are listed, where for graphene layers on metals that exhibit moiré patterns the closest separation is used. It is apparent that essentially only two separations are observed. For strongly interacting metals the graphene–metal separation is around 0.21 nm, while weakly interacting metals exhibit a separation of 0.33 nm, which is close to the distance of the van der Waals gap in graphite. The transition from strongly to weakly interacting transition metals can be correlated to the d-band center binding energy below the Fermi-level of the transition metals. As shown in Fig. 2, when we plot the substrate-graphene separation against the d-band center the transition from weakly to strongly interacting metals occurs at a d-band binding energy of ~2 eV. As we will describe below the interaction of the metal d-band with graphene results in a significant modification of the electronic structure of graphene. This will be discussed below for graphene–Ni(111). In contrast, the weakly interacting metals essentially only physisorb by van der Waals forces with the substrate and this leaves the electronic structure of graphene almost unaltered compared

Table 2 Graphene–metal separation and corresponding d-band center of the metals

	Graphene–metal separation [nm]	d-band center relative to Fermi-level according[23]
Co (0001)	0.21 (ref. 24)	−1.17
Ni (111)	0.21 (ref. 25)	−1.29
Cu (111)	0.33 (ref. 26 and 27)	−2.67
Ru (0001)	0.21 (ref. 28)	−1.41
Rh (111)	0.22 (ref. 29)	−1.73
Pd (111)	0.25 (ref. 30)	−1.83
Ag (111)	0.33 (ref. 26 and 27)	−4.30
Re (0001)	0.21 (ref. 31)	−0.51
Ir (111)	0.34 (ref. 32 and 33)	−2.11
Pt (111)	0.33 (ref. 7, 27, 30 and 32)	−2.25
Au (111)	0.33 (ref. 26, 27 and 32)	−3.56

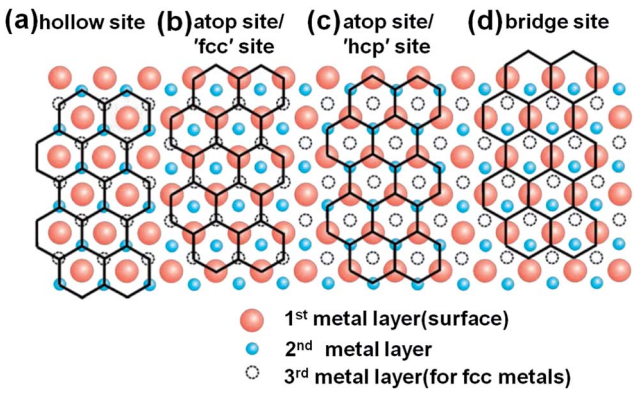

Fig. 1 The four different basic adsorption configurations of a honeycomb lattice on a lattice matched hexagonal densely packed metal surface.

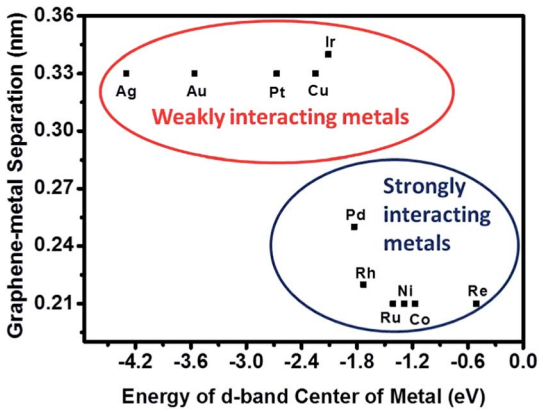

Fig. 2 Illustration of the correlation of graphene–metal separation with the energy of the d-band center of the transition metal. A transition from 'weak' to 'strong' interaction occurs at a d-band center position ~2 eV below the Fermi-level.

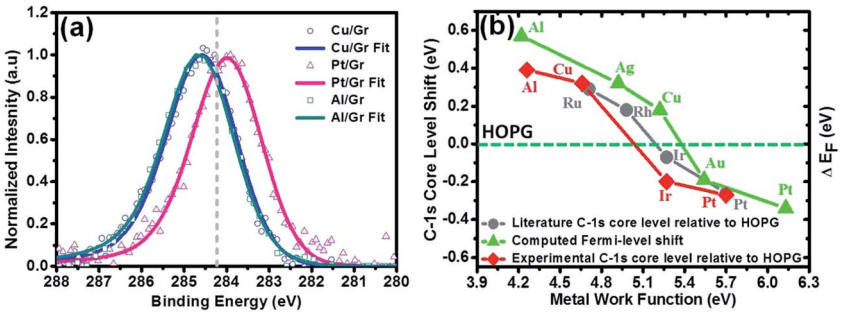

Fig. 3 Binding energy shift of C-1s core level on different weakly interacting metals and its correlation to charge transfer due to differences in work function of the metal and graphene. The schematic energy diagram shows the relationship between charge doping induced Fermi-level shift and measured C-1s core level in XPS. Adapted from ref. 22.

to that of free-standing graphene. Due to work function differences between the metal and graphene an interface charge transfer is observed, even for weakly interacting graphene. This causes doping of the graphene by the metal contact.[26] This doping effect can cause a shift of the Fermi-level of up to $\pm$0.3 eV relative to the graphene Dirac point. These shifts of the Fermi-level have been directly measured in angle resolved photoemission electron spectroscopy (ARPES) as $\sim$0.3 eV for Pt[7], $\sim$0.1 eV for Ir,[20] and ~ -0.3 eV for Cu,[21] where positive values correspond to a shift of the Fermi-level below the Dirac point. This interface charge transfer induced Fermi-level shift for weakly interacting metals can also explain the C-1s core level shift observed in X-ray photoemission spectroscopy (XPS).[22] In XPS the core-level is referenced to the Fermi-level and subsequently a shift of the Fermi-level will result in a concurrent core-level shift. Fig. 3 shows data of observed core level shifts as a function of metal work function. These core-level shifts are compared to computed Fermi-level shifts due to interface charge transfer between the metal and graphene. Obviously, the use of core-levels to determine the charge doping in graphene is only applicable to metals that interact by weak van der Waals interactions with graphene. For strongly interacting metals, like nickel, the C-1s binding energy of graphene is, however, not related to charge doping.

This review of the graphene–Ni interface is organized as follows: In the next chapter we discuss the physical properties of graphene on Ni, followed by a chapter on the thermal stability of carbon containing phases on Ni(111). In chapter 4 we discuss fundamental growth modes of graphene on Ni. We conclude this review in chapter 5 by giving examples of the use of Ni for the synthesis of complex graphene-based materials as well as potential uses of graphene–Ni interfaces.

2. Physical properties of graphene on nickel

2.1. Structure

Graphene on Ni(111). Monolayer graphene can be easily grown in ultra high vacuum (UHV) using hydrocarbon precursors, typically ethylene or propylene, with low pressures in the 10^{-9} to 10^{-6} Torr range. Different Ni(111) substrates have been used, varying from bulk single crystals[25,34–38] epitaxial Ni(111) layers on W(110)[39,40,41] to thin Ni-films on oxide substrates, such as Al_2O_3(0001),[42,43] MgO(111),[44] and YSZ (111).[42] The varying thickness of the these Ni-films and thus the amount of carbon that can be dissolved in them, as well as differing time to saturate these films with carbon at a given hydrocarbon pressures, may all influence the graphene growth. Those growth modes are discussed in chapter 4. Most reports of CVD-grown graphene under UHV indicate formation of a monolayer that is lattice matched with the Ni(111) surface. For a lattice-matched system different symmetry adsorption configuration are possible as illustrated in Fig. 1. The preferred arrangement of the graphene layer has been identified by LEED *I–V*[25] and ion scattering[45] studies as the structure with one carbon atom, of the two-carbon atoms in the primitive unit cell of graphene, located at the atop site and the second carbon atom located in the 'fcc' three-fold hollow site. The difference in the adsorption site of the two carbon atoms induces a buckling in the graphene lattice with the atop carbon displaced away from the surface and the atom in the three-fold hollow site closer to the Ni surface. Fig. 4 shows the interface structure determined from low energy electron diffraction (LEED) *I–V* measurements. A separation between Ni and graphene of 0.211 nm and a buckling of 0.005 nm has been deduced. These measurements are in good agreement with more recent density functional theory (DFT) analysis, which also suggest that the 'fcc' configuration is the most stable (strongest adsorbed) structure. The calculated work of adhesion for the 'fcc' structure is 0.81 J m^{-2}, compared to 0.77 J m^{-2} and 0.38 J m^{-2} for 'hcp' and 'hollow' adsorption configurations (see Fig. 1 for definition of adsorption structures), respectively.[35] The computed graphene-Ni(111) separation of 0.217 nm is very close to the experimental value, the buckling of the carbon atoms is somewhat smaller in DFT and a value of 0.003 nm is reported.[35] Although DFT suggests that the adsorption energy of graphene in the 'fcc' configuration is smaller than in the 'hcp' configuration the differences may be small enough so that both configurations may occur. Other reports also suggest that the 'bridge adsorption' structure is energetically accessible[46] and thus three different adsorption structures may be observed on Ni(111). As a consequence of graphene adsorbing in three possible adsorption configurations domain boundaries may form between these three

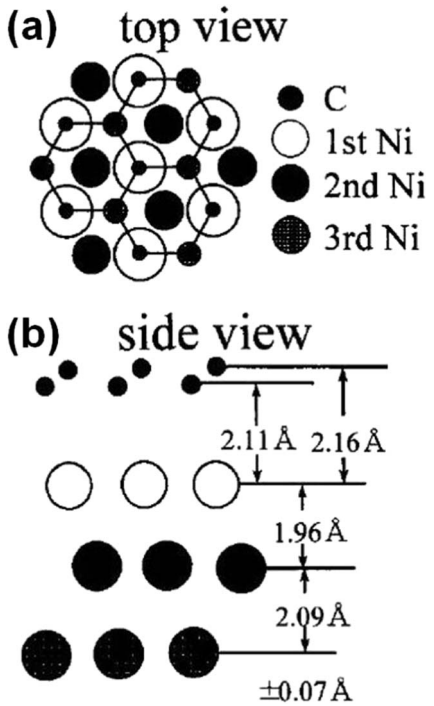

Fig. 4 Adsorption structure of graphene on Ni(111). (a) low symmetry adsorption structures. (b) Best fit structure for graphene on Ni(111) determined by LEED I(v). Reproduced from ref. 25.

configurations. The lattice matching conditions between two graphene domains whose unit-cells are translated such that one domain is in the 'fcc' structure and the other domain is in the 'hcp' structure may result in the formation of a reconstructed domain boundary as shown in Fig. 5(a). Such domain boundaries have been observed in scanning tunneling microscopy (STM)[47](as shown in Fig. 5(b)), clearly demonstrating the existence of graphene adsorbed with carbon in an 'fcc' site, as well as 'hcp' sites.

Under most imaging conditions in STM only one sublattice of the graphene is imaged for graphene on Ni(111). This means instead of imaging a honeycomb structure a triangular lattice is observed. This symmetry breaking is due to the two different adsorption sites of the carbon-atoms on the Ni(111) substrate, *i.e.* atop and hollow site. From the STM images of the domain boundary between an 'fcc' and 'hcp' domain, shown in Fig. 5, it is apparent that the carbon atoms located above the hollow sites are imaged brighter and the carbon atoms on the atop site are less bright.[47,48] This is opposite to the expected geometric buckling of the graphene-atoms.

For graphene grown under UHV conditions the dominant structure is monolayer graphene forming a lattice matched structure with Ni(111). However, the growth temperatures and potentially the substrate history (in particular carbon content in the substrate) may affect the growth. As discussed in chapter 4, under certain growth conditions, graphene sheets that are rotated with respect to the Ni(111) substrate are observed. Particularly at higher growth temperatures, and possibly related to a higher carbon concentration in the substrate, formation of graphene rotated relative to the Ni(111) substrate become more frequent. From LEED measurements it is apparent that a range of different rotation angles are possible, but a preferential rotation of $\sim 17^\circ \pm 7^\circ$ is observed. As expected, STM images of such rotated graphene show moiré structures, as for example shown in Fig. 6. In STM a corrugation of the moiré pattern with a peak-to-peak height of 0.2 Å is observed. This corrugation is smaller than that for graphene supported on other strongly interacting metal substrates (*e.g.* Ru, Re, or Rh) where

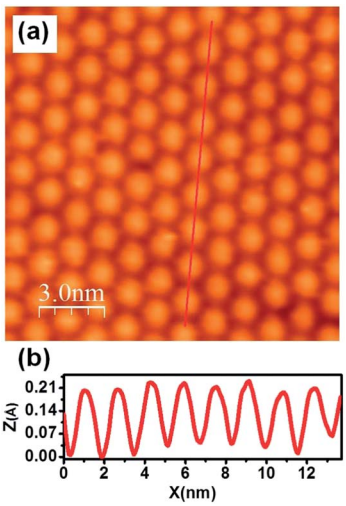

Fig. 6 STM image of rotated (twisted) graphene on Ni(111). A moiré-pattern is imaged in (a), note the long length scale. The line profile indicated by the red-line in (a) is plotted in (b).

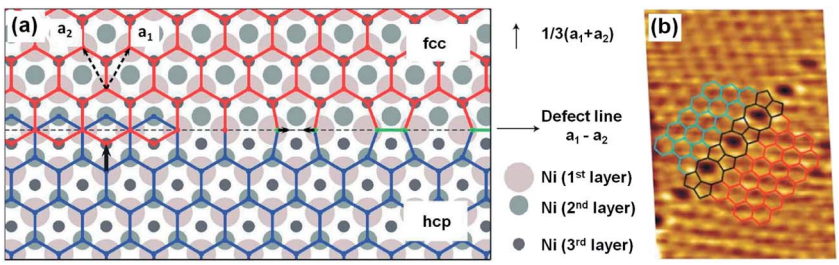

Fig. 5 Domain boundary in graphene translated by a fractional unit cell vector. This structure is formed on a Ni(111) substrate where graphene can adsorb with two adsorption geometries as schematically shown in (a). STM image in (b) shows the experimental verification of the existence of this domain boundary. Reproduced from ref. 47.

corrugations of ~1.1 to 1.6 Å are reported.[1] However, in the latter cases the low symmetry directions of graphene is aligned with the metal low symmetry direction and the moiré structure arises from the lattice mismatch between graphene and the metal. It may be argued that for rotated (or twisted) graphene no extended region of the graphene can be in sufficient registry with the metal substrate to form strong bonds and therefore the overall geometric corrugation of the graphene may be less than for a simple lattice mismatched case. Strong variations in the corrugation of the moiré pattern for graphene aligned (but lattice mismatched) and rotated with respect to the metal was also reported for graphene on Ir(111). For Ir(111) a value of 0.3 Å was reported for non-rotated graphene, while for graphene rotated by 30° the corrugation reduced to only 0.04 Å.[49] Further experiments and/or computation are needed to support the idea that the bonding between graphene and Ni(111) is strongly reduced for rotated (twisted) graphene and that this causes the lower corrugation than that commonly observed on strongly interacting metals.

For completeness, we also mention that similar STM measurements of moiré structures as those shown in Fig. 6 for graphene on nickel have been reported for ambient pressure CVD grown samples on polycrystalline Ni-films. In these cases the moiré structures were, however, interpreted as twisted bi-layer graphene.[50,51] In another study rotated monolayer graphene on Ni(111) facets was obtained by thermal treatment of Ni-clusters supported on HOPG.[52] In this case moiré patterns were also observed by STM and the moiré structures were assigned to graphene rotated by 6.4° and 23° relative to the Ni(111) lattice.

It is interesting to note here that regions of rotated graphene are preferential regions for nucleation and growth of either surface nickel carbide[53] or second layer graphene[54] at the interface between the graphene sheet and the nickel substrate by carbon segregation from the bulk. This is in agreement with the notion that graphene adsorbed in a 1 × 1 configuration, *i.e.* for graphene in a lattice matched registry with the Ni(111) substrate, is adsorbed much stronger than rotated graphene. The strongly adsorbed graphene may prevent carbon segregation to the surface while in regions of the weaker adsorbed rotated graphene carbon can segregate from the Ni-bulk more readily to form a new interface graphene sheet. Second layer graphene formation is discussed in the context of graphene synthesis in Section 4 in more detail.

Graphene on open Ni surfaces

Detailed UHV studies on the more open low index surfaces of Ni are rare. Comparative studies of carbon precipitation on different low index faces of carbon-saturated Ni-crystals by electron spectroscopy showed distinct behavior for the (100) surface[55] compared to (110) or (111).[56] While on the (110) and (111) nickel surfaces graphene forms at an abrupt temperature, on Ni(100) the carbon concentration at the surface increases smoothly as the temperature is lowered.

The only detailed structural studies of graphene monolayer on Ni single crystals, other than the (111) nickel surface, are on the (110) surface. On the (110) surface no commensurate structure between the rectangular surface unit cell of nickel can form with the hexagonal graphene lattice. LEED studies, shown in Fig. 7(a), indicate preferred orientation of the graphene. The graphene [1000] crystallographic direction is preferentially rotated by 12° with respect to the Ni[1$\bar{1}$0] direction. Two symmetry orientations are possible. However, as the arc-structure of the graphene LEED spots indicate, the rotation between graphene and Ni spans a few degrees. Consequently in STM imaging different moiré-superstructures may be observed. In Fig 7(b) an example for a 9.5° rotation angle is shown and a corresponding simulated image is shown in Fig 7(c).[57,58]

2.2. Electronic structure

Returning to the well-defined 1 × 1 lattice matched graphene layer on Ni(111). As the correlation between metal d-band binding energy and the graphene–metal separation shown in Fig. 2 suggests, the metal d-band may hybridize with the graphene and thus form a (weakly) chemisorbed system. This is clearly the case for nickel and detailed angle resolved photoemission spectroscopy (ARPES) and (polarization dependent) near edge X-ray absorption fine structure (NEXAFS) confirm the interaction between graphene and nickel. A detailed account of the electronic and magnetic structure of graphene on Ni has

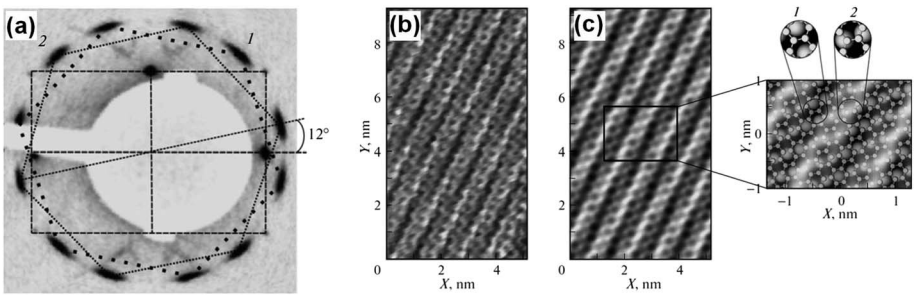

Fig. 7 LEED and STM characterization of graphene grown on Ni(110). The dashed line shows the reciprocal lattice of Ni(110), and the two dotted lines connect graphene diffraction spots of the two symmetry orientations. The arc structure of the graphene spots indicate a spread of possible orientations of the graphene lattice with respect to the Ni(110) substrate. An experimental STM image of graphene on Ni(110) is shown in (b). This may be compared to simulated STM image and ball-model for a 9.5° rotated graphene shown in (c). Reproduced from ref. 57.

been given previously by Dedkov and Fonin[59] and thus we only briefly discuss the most important details.

From ARPES measurements,[60–65] it is apparent that the electronic structure of graphene is strongly modified due to the interaction with Ni(111) compared to free-standing graphene. Fig. 8 shows an ARPES spectrum of graphene/Ni(111) and after gold-intercalation, which removes the Ni–graphene interaction. At the Γ-point the graphene π-band is observed at a binding energy (relative to the Fermi-energy) of 10.1 eV, which is ~2.4 eV lower than in graphite (or free-standing graphene). The graphene σ-states are also shifted to lower binding energies, however, by only 1.6 eV. This difference may indicate different hybridization between the Ni-3d states with the out-of plane π-orbitals compared to the in-plane σ-orbitals. Importantly, the graphene Dirac-cone, observed at the *K*-point in free-standing graphene is not preserved for graphene on nickel.

DFT simulations predicted a number of interface states between Ni(111) and graphene as a consequence of hybridization of Ni-3d with graphene π-states.[66,67] The existence of interface states was probed by polarization dependent NEXAFS measurements. Depending on the orientation of the electric field vector of the x-rays one can probe predominantly transitions from C-1s to σ*-states (orbitals lying within the graphene plane) or C-1s to π*-states (orbitals normal to the graphene plane). This polarization dependence is known as the 'search-light' effect. Fig. 9 shows experimental carbon *K*-edge NEXAFS spectra[68] for graphite, graphene–Ni(111), and after intercalation of Al in between graphene and Ni(111) which effectively decouples graphene from the Ni-substrate and forms quasi-free standing graphene. For the C-1s to π* transitions, the graphene–Ni(111) absorption spectra exhibits a double-peak structure compared to a single peak in graphite (or quasi free-standing graphene). This indicates two unoccupied interface states for graphene–Ni(111) as a consequence of the hybridization. The separation between the transitions to the π* and σ* decreases for graphene–Ni(111) compared to free-standing graphene. This is in agreement with a calculated shift of the σ* states by ~1 eV to lower binding energies, associated with a lateral carbon–carbon bond-softening in the adsorbed graphene.[69]

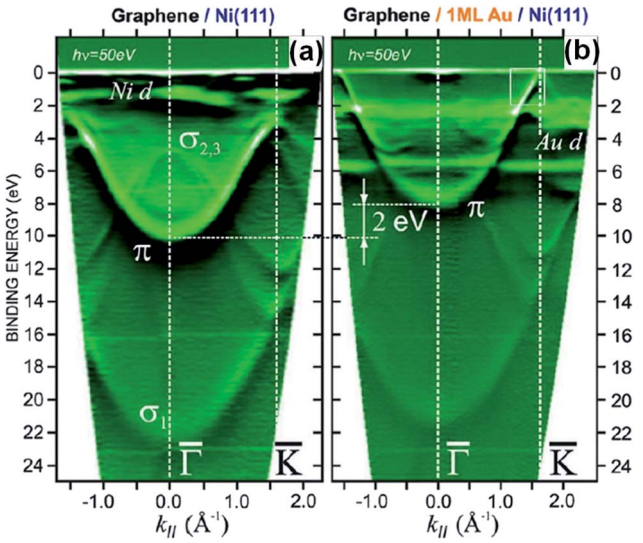

Fig. 8 ARPES measurement of graphene on Ni(111) (a) and graphene–Au–Ni(111) (b). For graphene on Ni the π band is downshifted by 2 eV. Intercalation of Au decouples graphene from the Ni substrate and forms electronically quasi-free standing graphene. Reproduced from ref. 65.

2.3. Magnetic properties

The magnetic properties of graphene monolayers on Ni(111) have been probed by spin polarized photoemission as well as by circular dichroism. Spin resolved photoemission studies appear to be controversial. One group is reporting an effective magnetic moment of carbon,[62] while another group disputes this claim.[70] Circular dichroism measurements in NEXAFS employs circular polarized light to measure the near edge X-ray absorption spectrum and thus enables tuning to an element specific absorption edge. The difference in X-ray absorption intensity between left- and right-polarized light gives information on the magnetic moment of this specific element. Carbon *K*-edge absorption spectra show a clear difference between the left and right polarized light for the 1s to π* transition while there is essentially no contrast in the 1s to σ* transition.[71,72] This suggests that only the π-orbitals of the graphene are magnetically polarized due to hybridization with the Ni-3d states of the substrate. Spin-polarized electronic structure calculations for the graphene–Ni(111) interface confirm the spin polarization of the graphene–nickel interface states. Fig. 10(a) illustrates the variations for minority and majority spin electron density at the interface.[68,73]

2.4. Phonon dispersion and absence of Raman signal

The phonon dispersion of graphene monolayers grown on Ni(111) has been measured by angle resolved high resolution electron energy loss spectroscopy (HREELS).[74,75] The strong interaction of graphene with nickel results in pronounced changes in the phonon spectrum compared to free-standing graphene or graphite. This has also been probed directly by comparing HREELS data for graphene–Ni(111) with the spectrum after 'decoupling' graphene form the nickel substrate by intercalating weakly interacting metals, such as copper,[76] silver,[77] or gold.[78] These experimental observations were summarized and discussed with the use of DFT simulations by Allard and Wirtz.[79] Fig. 11 shows the comparison between experimentally measured phonon dispersion and the computed results. We may distinguish between changes in the phonon dispersion due to stretching of the carbon bonds, required to match the Ni(111) lattice, and changes in the phonon spectrum as a direct consequence of the adsorption of graphene on Ni(111). The epitaxial lattice match between graphene and Ni, which results in a 1.5% stretching of the graphene bonds, leaves the acoustical and out-of-plane optical (ZO) mode almost unchanged. However, the longitudinal (LO) and transverse optical (TO) modes are strongly softened, *i.e.* the phonon frequency is shifted down by ~100 cm^{-1}. This softening is explained by a decrease in the stretching force constant due to

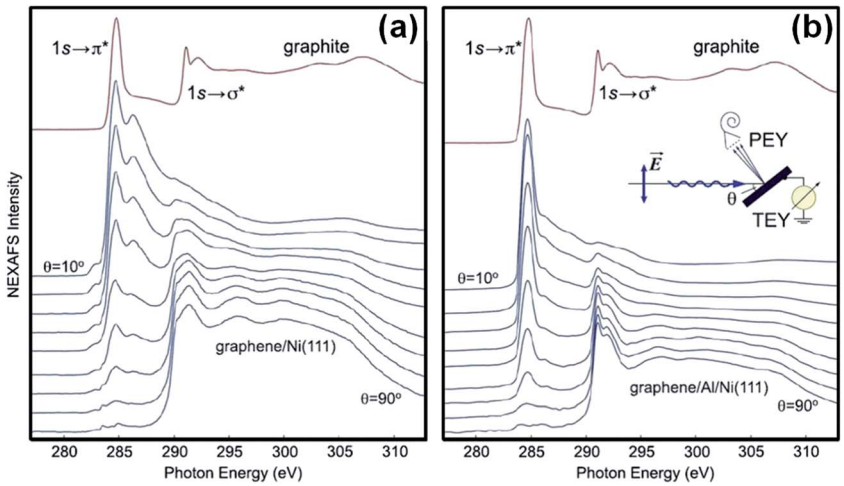

Fig. 9 Angle-dependent NEXAFS spectra of (a) graphene on Ni(111) and (b) graphene–Al–Ni(111) recorded at the carbon K-absorption edge. Spectra are recorded with different light-polarization by varying the incidence angle θ as indicated by the inset-cartoon. Upper part of each panel shows the NEXAFS spectrum of bulk graphite measured at $\theta = 30°$. Reproduced from ref. 68.

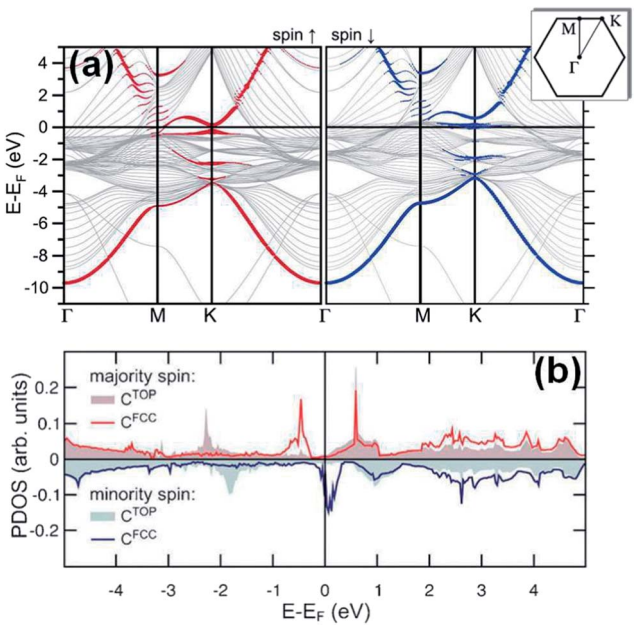

Fig. 10 (a) Spin-resolved electronic band structure of graphene on Ni(111) presented along Γ–M–K–Γ direction in the hexagonal Brillouin zone of graphene. The inset shows the corresponding Brillouin-zone for graphene. (b) Shows C-atom projected density of states for majority and minority spin. (a) and (b) are reproduced from ref. 68 and 73, respectively.

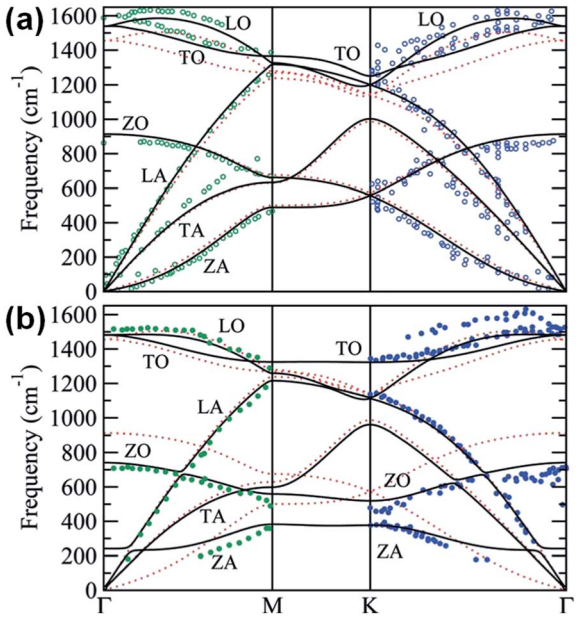

Fig. 11 Calculated (solid lines for graphene with lattice constant of graphite) and experimental (dots) phonon spectra for graphene/graphite (a) and graphene on Ni(111) (b). The red-dotted lines in both (a) and (b) is the computed phonon spectrum of free-standing graphene stretched by 1.5% to match the lattice constant of nickel. The experimental data are from ref. 81 (open green circles) ref. 82 (open blue circles), ref. 74 (filled green circles), and ref. 75 (filled blue circles). Figure reproduced from ref. 79.

the increase in the C–C bond length, while the unchanged acoustical and out-of-plane optical-mode indicates and unchanged bond-bending and bond-twisting force constant. The fact that the softening of the LO and TO mode are merely due to the change in the C–C bond length is shown computationally in Fig. 11(a) where the mode softening is reproduced by stretching the bonds without the presence of a substrate.

In addition to changes of the phonon modes due to the bond stretching significant changes occur due to chemical interaction, *i.e.* hybridization of the metal d-band with graphene π-states and charge transfer from the metal to graphene. Fig. 11(b) shows three major differences in the computed phonon spectrum of a 1.5% stretched free-standing graphene and the same structure adsorbed on Ni(111): (i) the ZO-mode is softened by 160 cm^{-1}, (ii) the degeneracy of the ZO and ZA modes at the K-point in the Brillouin zone is lifted and a

155 cm^{-1} gap is opened, and (iii) the highest optical branches (LO mode at Γ) and the (TO mode at K) become flat rather than displaying a kink (Kohn anomaly). The lifting of the degeneracy of ZO and ZA at the *K*-point is explained by the symmetry breaking of graphene on Ni(111) due to the alternating 'atop' and 'hollow' adsorption sites of carbon atoms in graphene–Ni(111). Also the downshift of the ZO branch is the consequence of the stronger interaction with the substrate. The disappearance of the Kohn anomaly, on the other hand, has its origin in the change of the electronic structure of nickel-supported graphene compared to freestanding graphene. The slope of the highest optical branch is a measure of the electron–phonon coupling between these modes and the π-bands in graphene. As discussed above, the hybridization of nickel d-electrons with graphene causes a downshift of the π-bands and opening of a gap. This annihilates electron-phonon coupling completely.

The electron–phonon coupling is critical for Raman spectroscopy. The chemical interaction between graphene and Ni leads to a large energy difference in the p_z orbitals of graphene and consequently a loss of the resonance conditions for Raman. Consequently, no Raman signal for graphene on Ni(111) is observed. Similarly for other strongly interacting metals such as Ru, no Raman signal is reported. Note that for Ru there is no lattice match between graphene and the substrate, further demonstrating that the loss of Raman is not a consequence of the stretching of the C–C bonds but a consequence of the electronic structure. This also implies that monolayer graphene on other nickel facets, or rotated graphene on Ni(111) should have a strongly suppressed Raman signal, as indeed observed in many experiments. Because Raman spectroscopy became the dominant characterization tool for graphene, the absence of a Raman signal for graphene–nickel may be an important warning that Raman is not a universal tool for graphene characterization. Despite the fundamental limitation of Raman there exist reports in the literature that assign a Raman to monolayer graphene on Ni.[80] Those reports should be taken with caution and may either indicate multi-layers or a decoupling of the graphene from the Ni due to impurities.

3. Carbon containing surface phases (carbide and graphene) on Ni and their thermal stability

In the catalysis and surface science community it has been known for some time that exposure of nickel surface to hydrocarbons can result in different carbon containing surface phases. In particular exposure of Ni(111) crystals to hydrocarbons at temperatures below 500 °C results in the formation of complex surface reconstruction. This structure was already identified in 1969 by LEED studies to exhibit a $\sqrt{39}\bar{R}\ 16.1^\circ \times \sqrt{39}R16.1^\circ$ periodicity with respect to the Ni(111) lattice, where $\bar{R}$ and R represent a rotation of the unit-cell vector of the superstructure in clock- and counter-clockwise direction, *i.e.* the unit cell is almost square with the two unit cell vectors enclosing an angle of 92.2° (60° + 2 × 16.1°).[15] The atomic model consists of smaller quasi-square units of a two-dimensional nickel carbide with a Ni_2C composition. This quasi-square nickel carbide overlayer on the hexagonal Ni(111) surface forms a coincidence structure with the unit cell vector length of $\sqrt{39}$ times the length of the surface lattice vector of Ni(111). Later STM studies, mainly confirmed the earlier LEED interpretation, however, the formation of a coincidence lattice structure was questioned.[16] Fig. 12, shows an STM image and a schematic illustration of this carbide layer.

Graphene is more carbon-dense compared to the Ni_2C phase and at growth temperatures below 600 °C forms a 1 × 1 structure with respect to Ni(111), *i.e.* the graphene is lattice matched with respect to Ni(111) as discussed above. The surface carbide and monolayer graphene can be easily distinguished by a variety of surface sensitive spectroscopy techniques. For instance in Auger spectroscopy the line shape for carbon, the C_{KVV} Auger line, is very distinct for the carbide and the graphene phase as is shown in Fig. 13. Also C-1s XPS can be used to distinguish graphene from carbide. For graphene on Ni(111) a C-1s peak position of 284.7–285.0 eV is observed[39,46,83] while for carbon in the Ni_2C surface phase a peak at 283.6 eV (ref. 46) or 283.2 eV (ref. 83) are reported. It is also worth mentioning that the graphene C-1s peak is strongly asymmetric and should be fitted with a Doniach-Sunjic lineshape.

Using these spectroscopic methods, as well as *in situ* microscopy such as low energy electron microscopy (LEEM), allows determination of the phase stability temperatures of Ni_2C and monolayer graphene on Ni(111). Preparing surfaces with the respective composition in UHV is achieved by exposure to low pressures (10^{-8} to 10^{-6} Torr) hydrocarbons. At sample temperatures of ~450 °C the surface carbide phase is readily formed while at temperatures of ~600 °C mainly graphene is obtained (a discussion of the growth mechanisms is presented in Section 4). The thermal stability of these surface phases on Ni single crystals can be tested. We emphasize that these studies were performed on bulk Ni crystals under UHV conditions,

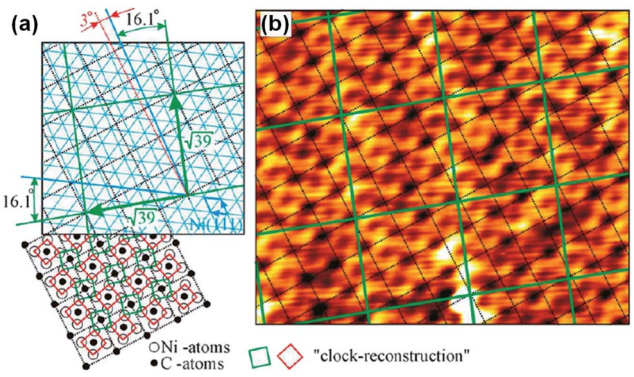

Fig. 12 Schematic model of a Ni_2C surface carbide on Ni(111) (a) and STM image of the surface carbide with unit-cell structure superimposed (b). In the model in (a) the blue lines indicate the Ni(111) lattice and the black dashed lines show the square building blocks of the surface nickel carbide. The unit cell vectors of the coincidence lattice between the carbide and the Ni(111) substrate is indicated by the green arrows. An atomic model showing the in-plane location of carbon and nickel atoms in the surface carbide is also shown. Reproduced from ref. 36.

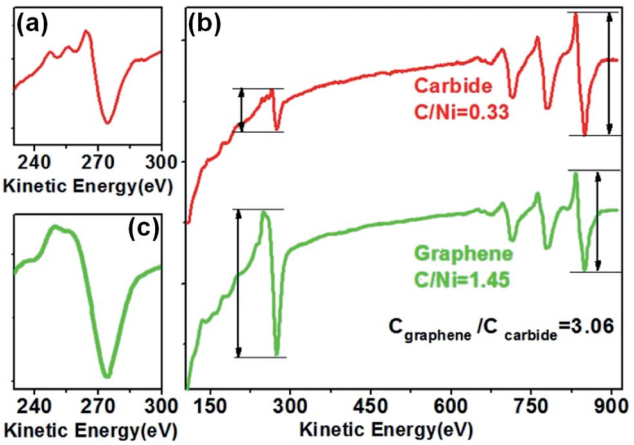

Fig. 13 : Auger electron spectra of monolayer carbide and monolayer graphene on a Ni(111) surface. (a) and (b) show the carbon-KVV Auger peak for carbide and graphene, respectively. (c) shows the carbon peak intensity in relation to the Ni-LMM peaks for carbide and graphene. Reproduced from ref. 35.

which as a consequence have very low carbon concentration in the nickel. This may be important, since the carbon concentration in the metal may affect the equilibrium between surface and the bulk and thus the phase stability of surface carbon phases. In Auger spectroscopy the disappearance of the carbon signal is observed for the surface carbide phase at ~480 °C and for the graphene monolayer at ~650 °C. The instability of graphene may also be appreciated from microscopy. Fig. 14(a), shows a LEEM image of an (incomplete) graphene layer at a sample temperature of 600 °C. At this temperature the graphene is stable. Raising the temperature to ~650 °C causes the graphene to disintegrate as the LEEM image of the same sample shows in Fig. 14(b).

The dependence of the stability of graphene at nickel surfaces on the carbon concentration in the bulk is apparent from the higher stability temperature of monolayer graphene reported by Blakely and co-workers.[84] In these studies a carbon

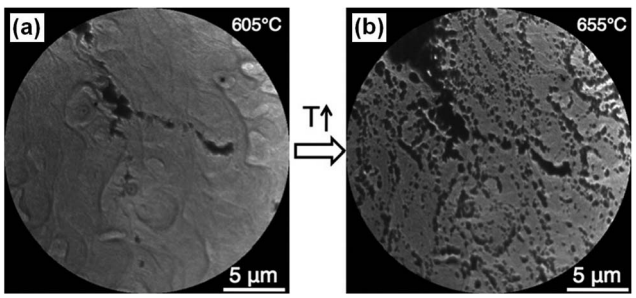

Fig. 14 Low energy electron microscopy (LEEM) study of the thermal stability of graphene–Ni(111). In (a) an incomplete graphene layer is shown (brighter contrast is due to graphene and the few dark areas are uncovered Ni substrate). The sample temperature is held at 605 °C and the graphene remains stable. In (b) the sample temperature is raised to 655 °C. The graphene is being etched and carbon dissolved into the bulk. It appears that initial 'attack' of the graphene preferentially occurs along Ni-step edges at the surface. Reproduced from ref. 34.

saturated Ni-crystal was heated to high temperatures in UHV. Auger spectroscopy was then used to determine the surface phases as they evolved during cooling. At high temperatures only dilute carbon atoms were detected at the surface. Monolayer graphene was observed by cooling to ~900 °C, *i.e.* at a significantly higher temperature than what is reported above for the phase stability temperature for graphene on (close to) pure Ni. In the Blakely experiment further cooling by another 100 K, *i.e.* to ~800 °C resulted in precipitation of carbon from the bulk to form graphite (multilayer graphene) at the surface.

4. CVD Growth of graphene on Ni

As the above discussion of phase stability temperatures suggest, the graphene growth mode may sensitively depend on the growth temperature. In particular, at high growth temperatures (>900 °C or higher, which are often employed in CVD-reactors or tube furnace growth), currently no direct evidence that (monolayer) graphene can be formed directly on Ni exists. However, cooling the sample from this high temperature will result in graphene and subsequently multilayer graphene will form by segregation and precipitation of carbon as the carbon solubility in the bulk decreases. In the Blakely experiments[84] of carbon-saturated Ni an upper temperature limit of ~900 °C for the stability of graphene was found under the specific conditions of their experiments. It is conceivable that further saturation (the saturation concentration is a function of temperature and thus the saturation-value depends on the preparation condition) of the Ni-bulk with carbon may increase the stability temperature further which may also lead to graphene formation at even higher temperatures. In any case, it would be challenging though to avoid carbon precipitation upon cooling for very high carbon concentrations in the nickel and thus graphitization of the surface would be difficult to suppress. In the temperature range between 650 °C and ~900 °C monolayer graphene has been demonstrated to be stable at the surface depending on concentration of carbon in the nickel-bulk. The lower temperature refers to the graphene stability temperature on a close-to carbon free nickel substrate. Even at these temperatures, if graphene is grown at higher hydrocarbon pressures (none-UHV conditions) it is difficult to suppress carbon precipitation upon cooling and therefore one expects multilayer graphene to form, unless special pre-cautions are taken to limit carbon diffusion to the surface. Nevertheless, some success has been demonstrated in achieving monolayer graphene growth even at fairly high growth temperatures and/or hydrocarbon exposures by limiting the amount of carbon precipitation by for example controlling Ni-film thickness, hydrocarbon exposure, and/or cooling rates.[14,85,86]

At temperatures below 650 °C monolayer graphene has been grown in UHV by many researchers (see chapter 2). Outside of a UHV chamber, in a more applied CVD setting the growth of monolayer graphene in registry with Ni(111) has to our knowledge not yet been demonstrated. We believe that the main challenge is two-fold: (i) it is more difficult to keep the Ni surface clean at lower temperature, in particular to avoid oxidation, and (ii) at higher hydrocarbon pressures more

carbon will dissolve into the bulk and thus multilayer formation upon cooling is more difficult to avoid. Thus the success for monolayer growth on Ni in a reactor setting seems to require achieving similar conditions as those in a UHV system, which may be possible in an appropriately sealed and pumped tube furnace. Therefore, the growth mechanisms studied in UHV may also have some technological relevance in the future. These UHV growth mechanisms are discussed, next.

Graphene growth on Ni(111) single crystals in UHV

UHV studies of graphene growth by exposure to ethylene (10^{-8} to 10^{-6} Torr) have been conducted at different sample temperatures and at least three different growth regimes may be differentiated.

(i) Below ~500 °C. At this temperature the above described Ni_2C surface phase forms rapidly at the surface. It has been suggested that this phase suppresses the nucleation of the more carbon dense graphene.[35] This may have two reasons: (i) the nickel carbide reduces the ability of the surface to activate the hydrocarbon precursor, *i.e.* reduced dehydrogenation of ethylene, and/or (ii) because the surface Ni_2C phase is a low energy line phase in a Ni–C surface-phase diagram any incorporation of additional carbon is associated with a large energy cost. Thus forming nuclei of graphene, which necessitate a higher carbon concentration within this carbide phase is associated with a large kinetic barrier. Nevertheless, probably at the numerous defects in the surface carbide, graphene eventually nucleates and grows. In electron spectroscopy it is observed that the carbide phase gradually transforms into graphene.[36,53] Also, the *in situ* high temperature STM studies[53] and low energy electron microscopy (LEEM)[34] confirmed the transformation of the surface carbide into graphene. In these *in situ* growth studies the formation of epitaxial graphene, *i.e.* graphene that is in registry with the Ni(111)-substrate was observed, contrary to the earlier reported notion that this transformation may result in the rotated graphene.[36] The *in situ* microscopy studies also showed that the growth front of the graphene domains is fragmented and this may lead to a rather defective graphene at these very low growth temperatures. A detailed investigation of the atomic defect structure in graphene as a function of growth mode by *e.g.* STM would be useful to correlate the LEEM studies with atomic defects. Such studies have not yet been reported.

(ii) Between 500 and 650 °C. In this temperature range no stable surface carbide is formed and graphene grows on predominantly pure Ni surfaces. In LEEM studies,[34] shown in Fig. 15, the presence of a not well-defined carbon containing phase is observed. The carbon of this phase is, however, consumed by the advancing graphene front, resulting a carbon-denuded zone in front of the graphene edge. Such a carbon gradient away from the growing graphene-edge suggests a surface diffusion driven growth of graphene by attachment of surface carbon species to the graphene edge. The growth of large, tens of micrometer diameter, graphene islands that grow across step edges is similar to the carpet-growth observed on other transition metal surfaces, where the graphene-sheet is

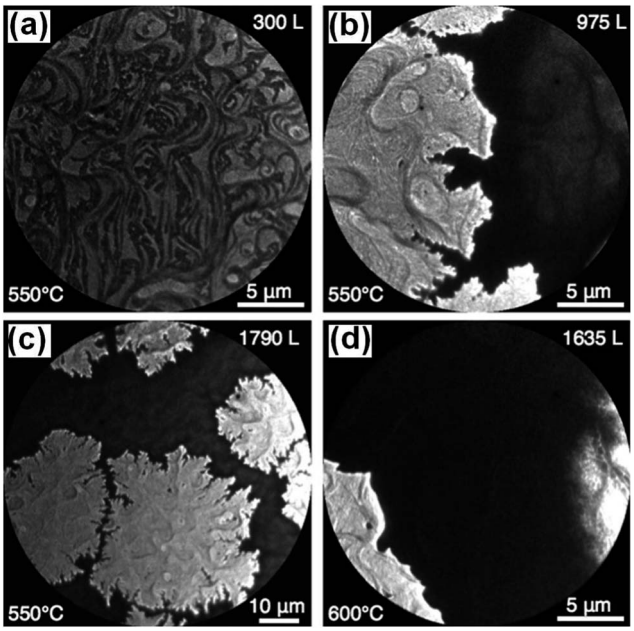

Fig. 15 LEEM images of surface structures at 550 °C (a)-(c) and 600 °C (d) for different ethylene exposures as indicated in the upper right corner of each image. Exposure to ethylene at 550 °C results in the formation of isolated carbide domains (a) for low ethylene exposure. Graphene growth is accompanied by formation of dark-contrast area in front of the graphene-edge (b). This zone is interpreted as a carbon denuded zone. A similar, but much wider zone, is formed at a growth temperature of 600 °C, evident in (d). A large area (77 μm field of view) is shown in (c) for 550 °C growth temperature. This view enables to assess the average graphene domain sizes before coalescence. Reproduced from ref. 34.

adsorbed on top of the metal and carbon-species attach to free-edges of the graphene. In particular step-edges do not present any significant obstacle for graphene in this growth mode for most metals. Only on Ru a higher barrier for step-up growth than for step-down growth has been reported.[6] Such a carpet growth of graphene on Ni(111), has, however, been recently disputed based on high temperature STM studies.[53] In these studies graphene growth on top of the metal was only observed for carbon contaminated substrate while for a clean Ni-surface graphene growth within the top most Ni surface layer has been observed, *i.e.* it has been proposed that the embedded graphene grows by replacement of Ni-atoms with carbon. Thus, according to these studies the dominant growth mode of graphene on Ni is different than on any other late transition metal. For Ru(0001)[87,88] and Rh[89] similar in-plane growth has been reported but only as a minority growth process. In the opinion of the authors of this review article the question if carpet-growth with 'free' graphene edges or graphene embedded in the top most Ni layer is the dominant growth mode is not unambiguously answered. Especially the role of carbon in the subsurface region is difficult to control but may significantly influence the growth mode.[53] Thus carbon concentration as well as other experimental parameters may give rise to seemingly contradicting results. While there may still be some discrepancies about the atomistic growth process in this temperature range, there exists

agreement that graphene forms on nickel without the presence of a carbide and graphene grows in a surface growth mode directly at the surface.

Most surface science studies have shown by a variety of structural probes, such as LEED,[25] ion scattering,[45] ARPES[60–63] and STM,[47,48,59] that at growth temperatures up to 650 °C the majority of the graphene is in registry with the Ni(111) surface. Contrary to this, a single recent study has suggested the presence of a majority structure of rotated graphene domains already at a growth temperature of 600 °C.[53] However, the studies of the authors of this review find by LEED and LEEM studies that the formation of majority of rotated graphene only occurs at higher growth temperatures. This is discussed next.

(iii) Between 650 and 800 °C. In order for graphene to remain stable on the nickel surface to temperatures higher than 650 °C and thus to enable growth at these higher temperatures, the nickel substrate has to have a high carbon concentration. This was discussed in chapter 3. In UHV this is best achieved on thin Ni-films, which can be easily saturated (note that ultrathin Ni-films on W(110) are not stable at these temperatures and thus Ni(111)-films on oxide supports are used). On ~300 nm thick Ni-films grown on YSZ(111) substrates, graphene was grown at temperatures up to ~800 °C in UHV. At these higher growth temperatures rotated graphene domains become more prevalent. The formation of rotated graphene has been systematically studied as a function of growth temperatures on Ni-films by LEED. Fig. 16(b) shows that at growth temperatures above 650 °C the LEED pattern indicates presence of a significant number of rotated graphene domains. It has also been observed directly in LEEM that upon cooling of the sample carbon from the bulk preferentially precipitates underneath of graphene domains that are rotated.[54] This results in bilayer formation underneath rotated graphene, which explains the higher C/Ni ratio in Auger spectroscopy shown in Fig. 16(c). Precipitation of carbon underneath of rotated graphene has also directly been observed in high temperature STM studies.[53] In the latter study a carbide was formed rather than graphene. This difference may be a consequence of the amount of carbon dissolved in the sample. Regardless, these direct *in situ* measurements of the growth demonstrate that the rotated graphene is formed first and subsequently the surface carbide and/or graphene is formed underneath by carbon segregation from the bulk. Thus an earlier suggestion that formation of the ordered surface-carbide facilitates the formation of rotated graphene[90] is not supported by these *in situ* measurements and consequently there exist no satisfying explanation for the formation of rotated graphene at higher growth temperatures and/or nickel films with higher carbon concentration.

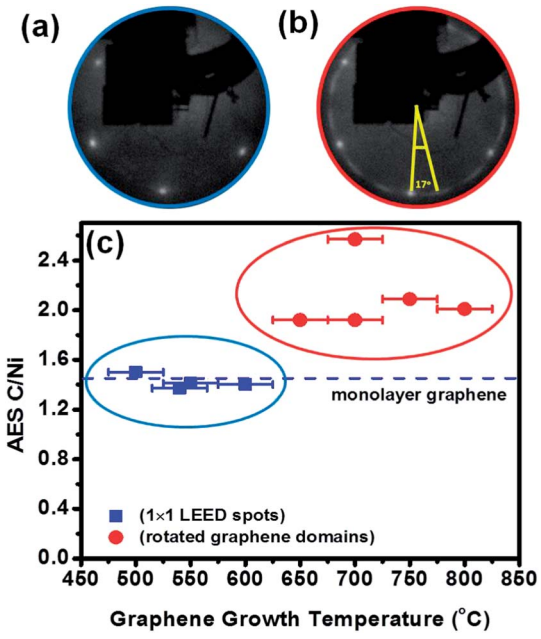

Fig. 16 Graphene growth on 300 nm thick Ni(111) film on YSZ(111). At growth temperatures above 650 °C rotated graphene-domains are observed in LEED. At the same time the C/Ni ratio measured by Auger electron spectroscopy indicate that bilayer graphene is present at the surface upon cooling for samples prepared at above 650 C. This demonstrates the correlation between rotated graphene and bilayer formation. Reproduced from ref. 54.

To summarize the growth of graphene in UHV: at temperatures below ~500 °C an ordered surface carbide is formed first that may transform to graphene if enough carbon is supplied. Between 500 and 650 °C graphene grows on pure Ni. To grow graphene directly at the surface at higher temperatures the carbon content in the substrate needs to be increased first. Once a high enough carbon concentration is established graphene may be grown at temperatures as high as 800–900 °C. However, at higher growth temperatures a significant fraction of the graphene is rotated with respect to the Ni(111) lattice. Carbon segregation from the bulk underneath these rotated graphene domains upon cooling either results in carbide or second layer graphene formation.

The observation of rotated graphene at higher growth temperatures even under UHV conditions seem to suggest that it is challenging to grow large area single grain graphene on Ni(111)-films in a high pressure, high temperature CVD reactor. Nevertheless, it is the opinion of the authors that in an appropriate reactor (a reactor that allows cleaning/reduction of the substrate by hydrogen followed by very low ethylene exposure at ~600 °C) single crystalline graphene monolayers may also be achievable in a non-traditional UHV chamber. Alternatively, modifying the growth procedures at ambient pressures may also enable to obtain mostly mono- or bilayer graphene by bulk carbon segregation.[91,92] Recently control of carbon concentration in Ni by post-carburization hydrogen etching and rapid cooling processes enabled fabrication of uniform graphene on polycrystalline Ni foils.[93] However, the improving success of growing large area graphene flakes on Cu[94] and the possibility of transferring graphene from weakly interacting noble metals such as Pt[95] without etching it may point into other directions than the use of nickel for obtaining large area high quality CVD grown graphene.

5. Complex graphene–Ni materials and potential applications of graphene–Ni interfaces

The above described fundamental properties form the foundation of more applied uses of nickel for the synthesis and application of graphene. Some of these areas in which the nickel–graphene interface is important are listed, here. Most of these applied materials are based on what has been described above and thus we restrict ourselves to a brief description of the application. This is not an exhaustive literature review, but rather gives a flavor of general uses for graphene–Ni compound materials.

While there are many other transition metals for the synthesis of graphene by CVD growth, some special materials properties of Ni may have advantages for synthesis of complex graphene-based materials. For instance, the high catalytic activity of Ni allow the growth of graphene or graphene-related sp^2 carbon structures at fairly low temperatures on pre-patterned Ni-films in order to form patterned graphene structures on substrates,[96] or by using porous Ni-scaffolds to form more complex 3D open network structures.[97,98] Etching of nickel with fairly benign chemicals allows removal of the metal and consequently leaving free-standing carbon structures behind.[99] Furthermore, the high carbon solubility of nickel in combination of its catalyzing-ability of sp^2 carbon may help to crystalizing graphene at nickel surfaces by diffusion of carbon through a nickel film.[100,101] This method appears to work for wide variety of solid carbon sources such as hydrocarbons,[102] amorphous carbon,[103,104] HOPG,[105] C_{60},[106] or diamond.[107] An improved control of monolayer graphene formation from solid carbon-sources was achieved by introduction of a diffusion barrier between the Ni-film and the carbon source.[108] In addition, high temperature evaporation of the nickel catalyst may be used to just leave the graphene behind on a dielectric support without the presence of the metal.[109] Finally, graphitization of a self-assembled monolayer on an oxide support by a top deposited Ni-film was demonstrated.[110]

Nickel may also be a good material for making efficient electric contact to graphene. The strong chemical interaction between graphene and nickel may improve the contact. More importantly, though, nickel can easily chemically attack the graphene. Commonly, if a metal is deposited onto graphene to make a contact only 'top-contacts' are formed where the metal sits on a perfect graphene sheet. However, it has been shown that 'side-contacts', *i.e.* contacts where metals interact with graphene edges, can lower the contact resistance.[111] If a reactive metal like Ni is deposited holes in the graphene may form. This may lead to formation of bonds between graphene-edges and nickel and consequently formation of in-plane or 'side-contacts' to the graphene.[112] This has the potential of lowering the contact resistances without the need of pre-patterning the graphene.[113]

The high reactivity of Ni and its ability to 'soak' up excess carbon can also be utilized to etch graphene either just by pure nickel or by addition of another etchant that is activated at the Ni surface, *e.g.* hydrogen.[114,115]

A single graphene layer on Ni, like on other metals, can protect the Ni-surface from corrosion.[116–118] This is a useful property, especially for a material like Ni that easily oxidizes when exposed to atmospheric conditions. This property may be exploited in fabrication of metal/oxide heterolayers, for instance in the production of efficient magneto-tunnel junctions in spin-valves.[42,119,120] A graphene layer on a Ni-film may protect it from oxidation during growth of the oxide dielectric and this may results in a sharper metal/oxide interface.[121] It may also be proposed that subsequent high temperature annealing may be used to dissolve the graphene in the Ni if desired. A related but not well studied field is the use of a graphene protective 'coatings' on Ni or other transition metals in (electro) chemical applications for protection of electrodes/catalysts from corrosion.

Finally, CVD-grown graphene on Ni may just be the initial material. The nickel substrate may be subsequently modified. It has been shown that a large number of physical-vapor deposited elements can be intercalated between graphene and Ni at fairly low temperatures (typically below 400 °C). Depending on the annealing temperature and the miscibility of the deposited element with nickel, the deposited materials may form an ad-layer between graphene and Ni,[75,77,78,122] or alloy with the substrate. This allows forming graphene interfaces with many other pure-metals or alloys[123] and compounds (such as nickel silicide[124]).

6. Summary

The fundamental physical properties of the graphene–Ni(111) interface are quite well understood. Strong chemical interaction between the Ni and graphene results in a hybridization of the d-band with the π-states of graphene. This causes a ~2.4 eV down ward shift of the π-states and opening of a gap in graphene. Hybridization and charge transfer induces a magnetic moment on the carbon atoms. Stretching of the C–C bond of graphene on Ni(111), symmetry breaking in the graphene structure, and strong adsorption of carbon to the substrate causes a change in the phonon dispersion of graphene supported on Ni(111) compared to free-standing graphene or graphite. The change in the electronic structure of graphene due to the adsorption on nickel suppresses the Kohn anomalies in the phonon dispersion and as a consequence no Raman signal is observed for monolayer graphene on nickel.

The fundamental CVD growth mechanisms of graphene on Ni(111) was carefully studied by ultrahigh vacuum surface science techniques. Electron spectroscopy as well as *in situ* microscopy (STM and LEEM) enabled detailed understanding of the growth modes. Depending on the sample temperatures (and potentially the carbon concentration in the nickel substrate) different growth modes have been identified. At low temperatures graphene formation competes with the presence of a surface carbide phase and graphene forms by a transformation of the carbide. In an intermediate temperature range from 500–650 °C graphene grows in two-dimensional surface growth mode. This temperature range can be increased by increasing the carbon concentration in the bulk. However, in

addition to graphene that is lattice matched with the Ni(111) surface, domains of graphene that are rotated with respect to Ni(111) appear more frequent at higher temperatures/higher carbon content in the bulk. Those rotated domains are preferential regions for subsequent carbon segregation from the bulk, forming either bi-layer graphene or graphene supported on a surface nickel carbide. As early studies by Blakely *et al.* showed,[56,84] carbon saturated Ni-crystals only exhibit graphene formation upon cooling to below 900 °C. At higher temperatures carbon remains dissolved in the bulk. This suggests that in order to grow graphene at such high temperatures the nickel needs to be saturated by carbon first before graphene can form. For a high concentration of carbon in the bulk it appears challenging to suppress precipitation upon cooling and thus under most sample and cooling conditions this will result in multilayer formation for nickel samples exposed to hydrocarbons at temperatures of 900 °C or higher.

Controlled CVD growth of graphene on nickel under non-UHV conditions remains a challenge. At the same time, the success of other transition metals, in particular copper, for the synthesis of graphene and the possibility of transfer of graphene from precious metals such as platinum, without etching the material suggests that nickel may not play an important role in the synthesis of large scale wafer-sized graphene for electronics applications. On the other hand, nickel has advantages for low temperature synthesis of graphene and/or of irregularly shaped porous graphene materials by using nickel foams and similar Ni-materials as scaffolds. Also the high carbon solubility and carbon diffusivity that hampers direct monolayer graphene growth, may be advantageous in transforming carbon deposits into ordered graphene, by absorbing and re-segregation of carbon. The strong-interaction between nickel and graphene make these interfaces also potentially useful for electrical contacts between graphene and metals.

Acknowledgements

Financial support from the National Science Foundation under grant DMR-1204924 is acknowledged.

References

1 M. Batzill, *Surf. Sci. Rep.*, 2012, **67**, 83–115.
2 J. Wintterlin and M. L. Bocquet, *Surf. Sci.*, 2009, **603**, 1841–1852.
3 X. Li, W. Cai, J. An, S. Kim, J. Nah, D. Yang, R. Piner, A. Velamakanni, I. Jung, E. Tutuc, S. K. Banerjee, K. Sanjay, L. Colombo and R. S. Ruoff, *Science*, 2009, **324**, 1312–1314.
4 S. Bae, H. Kim, Y. Lee, X. F. Xu, J. S. Park, Y. Zheng, J. Balakrishnan, T. Lei, H. R. Kim, Y. I. Song, Y. J. Kim, K. S. Kim, B. Ozyilmaz, J. H. Ahn, B. H. Hong and S. Iijima, *Nat. Nanotechnol.*, 2010, **5**, 574–578.
5 J. Coraux, A. T. N'Diaye, M. Engler, C. Busse, D. Wall, N. Buckanie, F. J. M. zu Heringdorf, R. van Gastel, B. Poelsema and T. Michely, *New J. Phys.*, 2011, **11**, 023006.
6 P. W. Sutter, J. I. Flege and E. A. Sutter, *Nat. Mater.*, 2011, **7**, 406–411.
7 P. Sutter, J. T. Sadowski and E. Sutter, *Phys. Rev. B: Condens. Matter Mater. Phys.*, 2009, **80**, 245411.
8 P. Sutter and E. Sutter, *Adv. Funct. Mater.*, 2013, **23**, 2617–2634.
9 T. Oznuluer, E. Pince, E. O. Polat, O. Balci, O. Salihoglu and C. Kocabas, *Appl. Phys. Lett.*, 2011, **98**, 183101.
10 S. Nie, N. C. Bartelt, J. M. Wofford, O. D. Dubon, K. F. McCarty and K. Thurmer, *Phys. Rev. B: Condens. Matter Mater. Phys.*, 2012, **85**, 205406.
11 J. M. Wofford, E. Starodub, A. L. Walter, S. Nie, A. Bostwick, N. C. Bartelt, K. Thuermer, E. Rotenberg, K. F. McCarty and O. D. Dubon, *New J. Phys.*, 2012, **14**, 053008.
12 X. Li, W. Cai, L. Colombo and R. S. Ruoff, *Nano Lett.*, 2009, **9**, 4268–4272.
13 L. Gao, W. Ren, H. Xu, L. Jin, Z. Wang, T. Ma, L.-P. Ma, Z. Zhang, Q. Fu, L.-M. Peng, X. Bao and H.-M. Cheng, *Nat. Commun.*, 2012, **3**, 699.
14 R. S. Weatherup, B. Dlubak and S. Hofmann, *ACS Nano*, 2012, **6**, 9996–10003.
15 J. J. McCarroll, T. Edmonds and R. C. Pitkethly, *Nature*, 1969, **223**, 1260–1262.
16 C. Klink, I. Stensgaard, F. Besenbacher and E. Lægsgaard, *Surf. Sci.*, 1995, **342**, 250–260.
17 C.-M. Sung and M.-F. Tai, *Int. J. of Refractory Metals & Hard Mater.*, 1997, **15**, 237–256.
18 Z. R. Robinson, P. Tyagi, T. R. Mowll, C. A. Ventrice Jr and J. B. Hannon, *Phys. Rev. B: Condens. Matter Mater. Phys.*, 2012, **86**, 235413.
19 P. Merino, M. Svec, A. L. Pinardi, G. Otero and J. A. Martin-Gago, *ACS Nano*, 2011, **5**, 5627–5634.
20 I. Pletikosić, M. Kralj, P. Pervan, R. Brako, J. Coraux, A. T. N'Diaye, C. Busse and T. Michely, *Phys. Rev. Lett.*, 2009, **102**, 056808.
21 A. L. Walter, S. Nie, A. Bostwick, K. S. Kim, L. Moreschini, Y. J. Chang, D. Innocenti, K. Horn, K. F. McCarty and E. Rotenberg, *Phys. Rev. B: Condens. Matter Mater. Phys.*, 2011, **84**, 195443.
22 A. Dahal, R. Addou, H. Coy-Diaz, J. Lallo and M. Batzill, *APL Mater.*, 2013, **1**, 042107.
23 B. Hammer and J. K. Norskov, *Adv. Catal.*, 2000, **45**, 71–129.
24 D. Eom, D. Prezzi, K. T. Rim, H. Zhou, M. Lefenfeld, S. Xiao, C. Nuckolls, M. S. Hybertsen, T. F. Heinz and G. W. Flynn, *Nano Lett.*, 2009, **9**, 2844–2848.
25 Y. Gamo, A. Nagashima, M. Wakabayashi, M. Terai and C. Oshima, *Surf. Sci.*, 1997, **374**, 61–64.
26 G. Giovannetti, P. A. Khomyakov, G. Brooks, V. M. Karpan, J. van den Brink and P. J. Kelly, *Phys. Rev. Lett.*, 2008, **101**, 026803.
27 M. Vanin, J. Mortensen, A. K. Kelkkanen, J. M. Garcia-Lastra, K. S. Thygesen and K. W. Jacobsen, *Phys. Rev. B: Condens. Matter Mater. Phys.*, 2010, **81**, 081408(R).
28 W. Moritz, B. Wang, M.-L. Bocquet, T. Brugger, T. Gerber, J. Wintterlin and S. Günther, *Phys. Rev. Lett.*, 2010, **104**, 136102.
29 B. Wang, M. Caffiom, C. Bromley, H. Früchtl and R. Schaub, *ACS Nano*, 2010, **4**, 5773–5782.

30 Q. J. Wang and J. G. Che, *Phys. Rev. Lett.*, 2009, **103**, 066802.
31 E. Miniussi, M. Pozzo, A. Baraldi, E. Vesselli, R. R. Zhan, G. Comelli, T. O. Menteş, M. A. Niño, A. Locatelli, S. Lizzit and D. Alfè, *Phys. Rev. Lett.*, 2011, **106**, 216101.
32 C. Gong, G. Lee, B. Shan, E. M. Vogel, R. M. Wallace and K. Cho, *J. Appl. Phys.*, 2010, **108**, 123711.
33 C. Busse, P. Lazic, R. Dejemour, J. Coraux, T. Gerber, N. Atodiresei, V. Caiuc, R. Brako, A. T. N'Diaye, S. Buegel, J. Zegenhagen and T. Michely, *Phys. Rev. Lett.*, 2011, **107**, 036101.
34 R. Addou, A. Dahal, P. Sutter and M. Batzill, *Appl. Phys. Lett.*, 2012, **100**, 021601.
35 J. Lahiri, T. S. Miller, A. J. Ross, L. Adamska, I. I. Oleynik and M. Batzill, *New J. Phys.*, 2011, **13**, 025001.
36 J. Lahiri, T. Miller, L. Adamska, I. I. Oleynik and M. Batzill, *Nano Lett.*, 2011, **11**, 518–522.
37 A. M. Shikin, V. K. Adamchuk and K. H. Rieder, *Phys. Solid State*, 2009, **51**, 2390–2400.
38 A. M. Shikina, D. Faríasb, V. K. Adamchuka and K.-H. Rieder, *Surf. Sci.*, 1999, **424**, 155–167.
39 A. Grüneis, K. Kummer and D. V. Vyalikh, *New J. Phys.*, 2009, **11**, 073050.
40 Yu. S. Dedkov, M. Fonin and C. Laubschat, *Appl. Phys. Lett.*, 2008, **92**, 052506.
41 M. Weser, Y. Rehder, K. Horn, M. Sicot, M. Fonin, A. B. Preobrajenski, E. N. Voloshina, E. Goering and Y. S. Dedkov, *Appl. Phys. Lett.*, 2010, **96**, 012504.
42 A. Dahal, H. Coy-Diaz, R. Addou, J. Lallo, E. Sutter and M. Batzill, *J. Appl. Phys.*, 2013, **113**, 194305.
43 D. L. Miller, M. W. Keller, J. W. Shaw, A. N. Chiaramonti and R. R. Keller, *J. Appl. Phys.*, 2012, **112**, 064317.
44 T. Iwasaki, H. J. Park, M. Konuma, D. S. Lee, J. H. Smet and U. Starke, *Nano Lett.*, 2011, **11**, 79–84.
45 H. Kawanowa, H. Ozawa, T. Yazaki, Y. Gotoh and R. Souda, *Jpn. J. Appl. Phys.*, 2002, **41**, 6149–6152.
46 W. Zhao, S. M. Kozlov, O. Hoefert, K. Gotterbarm, M. P. A. Lorenz, F. Vines, C. Papp, A. Goerling and H. P. Steinrück, *J. Phys. Chem. Lett.*, 2011, **2**, 759–764.
47 J. Lahiri, Y. Lin, P. Bozkurt, I. I. Oleynik and M. Batzill, *Nat. Nanotechnol.*, 2010, **5**, 326–329.
48 L. V. Dzemiantsova, M. Karolak, F. Lofink, A. Kubetzka, B. Sachs, K. von Bergmann, S. Hankemeier, T. O. Wehling, R. Frömter, H. P. Oepen, A. I. Lichtenstein and R. Wiesendanger, *Phys. Rev. B: Condens. Matter Mater. Phys.*, 2011, **84**, 205431.
49 E. Loginova, S. Nie, K. Thürmer, N. C. Bartelt and K. F. McCarty, *Phys. Rev. B: Condens. Matter Mater. Phys.*, 2009, **80**, 085430.
50 R. Zhao, Y. Zhang, T. Gao, Y. Gao, N. Liu, L. Fu and Z. Liu, *Nano Res.*, 2011, **4**, 712–721.
51 Y. Zhang, T. Gao, S. Xie, B. Dai, L. Fu, Y. Gao, Y. Chen, M. Liu and Z. Liu, *Nano Res.*, 2012, **5**, 402–411.
52 Y. Murata, V. Petrova, B. B. Kappes, A. Ebnonnasir, I. Petrov, Y. H. Xie, C. V. Ciobanu and S. Kodambaka, *ACS Nano*, 2010, **4**, 6509–6514.
53 L. L. Patera, C. Africh, R. S. Weatherup, R. Blume, S. Bhardwaj, C. Castellarin-Cudia, A. Knop-Gericke, R. Schloegl, G. Comelli, S. Hofmann and C. Cepek, *ACS Nano*, 2013, **7**, 7901–7912.
54 A. Dahal, R. Addou, P. Sutter and M. Batzill, *Appl. Phys. Lett.*, 2012, **100**, 241602.
55 J. M. Blakely, J. S. Kim and H. C. Potter, *J. Appl. Phys.*, 1970, **41**, 2693–2697.
56 M. Eizenberg and J. M. Blakely, *J. Chem. Phys.*, 1979, **71**, 3467–3477.
57 A. V. Fedorov, A. Yu. Varykhalov, A. M. Dobrotvorskii, A. G. Chikina, V. K. Adamchuk and D. Yu. Usachov, *Phys. Solid State*, 2011, **53**, 1952–1956.
58 D. Usachov, A. M. Dobrotvorskii, A. Varykhalov, O. Rader, W. Gudat, A. M. Shikin and V. K. Adamchuk, *Phys. Rev. B: Condens. Matter Mater. Phys.*, 2008, **78**, 085403.
59 Yu. S. Dedkov and M. Fonin, *New J. Phys.*, 2010, **12**, 125004.
60 A. Nagashima, N. Tejima and C. Oshima, *Phys. Rev. B: Condens. Matter Mater. Phys.*, 1994, **50**, 17487.
61 Yu. S. Dedkov, A. M. Shikin, V. K. Adamchuk, S. Molodtsov, C. Laubschat, A. Bauer and G. Kaindl, *Phys. Rev. B: Condens. Matter Mater. Phys.*, 2001, **64**, 035405.
62 Yu. S. Dedkov, M. Fonin, U. Rüdiger and C. Laubschat, *Phys. Rev. Lett.*, 2008, **100**, 107602.
63 A. M. Shikin, G. V. Prudnikova, V. K. Adamchuk, F. Moresco and K. H. Rieder, *Phys. Rev. B: Condens. Matter Mater. Phys.*, 2000, **62**, 13202.
64 A. Grüneis and D. Vyalikh, *Phys. Rev. B: Condens. Matter Mater. Phys.*, 2008, **77**, 193401.
65 A. Varykhalov, J. Sánchez-Barriga, A. M. Shikin, C. Biswas, E. Vescovo, A. Rybkin, D. Marchenko and O. Rader, *Phys. Rev. Lett.*, 2008, **101**, 157601.
66 V. M. Karpan, P. A. Khomyakov, A. A. Starikov, G. Giovannetti, M. Zwierzycki, M. Talanana, G. Brocks, J. van den Brink and P. J. Kelly, *Phys. Rev. B: Condens. Matter Mater. Phys.*, 2008, **78**, 195419.
67 G. Bertoni, L. Calmels, A. Altibelli and V. Servin, *Phys. Rev. B: Condens. Matter Mater. Phys.*, 2005, **71**, 075402.
68 E. N. Voloshina, A. Generalov, M. Weser, S. Böttcher, K. Horn and Yu. S. Dedkov, *New J. Phys.*, 2011, **13**, 113028.
69 E. Voloshina, R. Ovcharenko, A. Schulakov and Yu. Dedkov, *J. Chem. Phys.*, 2013, **138**, 154706.
70 O. Rader, A. Varykhalov, J. Sanches-Barriga, D. marchenko, A. Rybkin and A. M. Shikin, *Phys. Rev. Lett.*, 2009, **102**, 057602.
71 M. Weser, Y. Rehder, K. Horn, M. Sicot, M. Fonin, A. B. Preobrajenski, E. N. Voloshina, E. Goering and Yu. S. Dedkov, *Appl. Phys. Lett.*, 2010, **96**, 012504.
72 Yu. S. Dedkov, M. Sicot and M. Fonin, *J. Appl. Phys.*, 2010, **107**, 09E121.
73 M. Weser, E. N. Voloshina, K. Horn and Yu. S. Dedkov, *Phys. Chem. Chem. Phys.*, 2011, **13**, 7534–7539.
74 T. Aizawa, R. Souda, Y. Ishizawa, H. Hirano, T. Yamada, K. Tanaka and C. Oshima, *Surf. Sci.*, 1990, **237**, 194–202.
75 A. M. Shikin, D. Farías, V. K. Adamchuk and K.-H. Rieder, *Surf. Sci.*, 1999, **424**, 155–167.
76 A. M. Shikin, D. Farías and K. H. Rieder, *Europhys. Lett.*, 1998, **44**, 44–49.

77 D. Farías, K. H. Rieder, A. M. Shikin, V. K. Adamchuk, T. Tanaka and C. Oshima, *Surf. Sci.*, 2000, **454-456**, 437–441.
78 A. M. Shikin, G. V. Prudnikova, V. K. Adamchuk, F. Moresco and K.-H. Rieder, *Phys. Rev. B: Condens. Matter Mater. Phys.*, 2000, **62**, 13202–13208.
79 A. Allard and L. Wirtz, *Nano Lett.*, 2010, **10**, 4334–4340.
80 K. S. Kim, Y. Zhao, H. Jang, S. Y. Lee, J. M. Kim, K. S. Kim, J.-H. Ahn, P. Kim, J. Y. Choi and B. H. Hong, *Nature*, 2009, **457**, 706–710.
81 C. Oshima, T. Aizawa, R. Souda, Y. Ishizawa and Y. Sumiyoshi, *Solid State Commun.*, 1988, **65**, 1601–1604.
82 S. Siebentritt, R. Pues, K.-H. Rieder and A. M. Shikin, *Phys. Rev. B: Condens. Matter Mater. Phys.*, 1997, **55**, 7927–7934.
83 R. S. Weatherup, B. C. Bayerm, R. Blume, C. Baehtz, P. R. Kidambi, M. Fouquet, C. T. Wirth, R. Schlögel and S. Hofmann, *Chem. Phys. Chem.*, 2012, **13**, 2544–2549.
84 J. C. Shelton, H. R. Patil and J. M. Blakely, *Surf. Sci.*, 1974, **43**, 493–520.
85 A. Reina, S. Thiele, X. Jia, S. Bhaviripudi, M. S. Dresselhaus, J. A. Schaefer and J. Kong, *Nano Res.*, 2009, **2**, 509–516.
86 J. H. Chu, J. Kwak, T.-Y. Kwon, S.-D. Park, H. Go, A. Y. Kim, K. Park, S. Kang and S.-Y. Kwon, *ACS Appl. Mater. Interfaces*, 2012, **4**, 1777–1782.
87 S. G. Günther, S. Dänhardt, B. Wang, M.-L. Bocquet, S. Schmitt and J. Wintterlin, *Nano Lett.*, 2011, **11**, 1895–1900.
88 E. Starodub, S. Maier, I. Stass, N. C. Bartelt, P. J. Feibelman, M. Salmeron and K. F. McCarty, *Phys. Rev. B: Condens. Matter Mater. Phys.*, 2009, **80**, 235422.
89 G. C. Dong, D. W. van Baarle, M. J. Rost and J. W. M. Frenken, *New J. Phys.*, 2012, **14**, 053033.
90 P. Jacobson, B. Stoger, A. Garhofer, G. S. Parkinson, M. Schmid, R. Caudillo, F. Mittendorfer, J. Redinger and U. Diebold, *ACS Nano*, 2012, **6**, 3564–3572.
91 L. Huang, Q. H. Chang, G. L. Guo, Y. Liu, Y. Q. Xie, T. Wang, B. Ling and H. F. Yang, *Carbon*, 2012, **50**, 551–556.
92 C. C. Lu, C. Jin, Y.-C. Lin, C.-R. Huang, K. Suenga and P.-W. Chiu, *Langmuir*, 2011, **27**, 13748.
93 Y. Gong, X. Zhang, G. Liu, L. Wu, X. Geng, M. Long, X. Cao, Y. Guo, W. Li, J. Xu, M. Sun, L. Lu and L. Liu, *Adv. Funct. Mater.*, 2012, **22**, 3153–3159.
94 X. S. Li, C. W. Magnuson, A. Venugopal, R. M. Tromp, J. B. Hannon, E. M. Vogel, L. Colombo and R. S. Ruoff, *J. Am. Chem. Soc.*, 2011, **133**, 2816–2819.
95 L. B. Gao, W. C. Ren, H. L. Xu, L. Jin, Z. X. Wang, T. Ma, L. P. Ma, Z. Y. Zhang, Q. Fu, L. M. Peng, X. H. Bao and H. M. Cheng, *Nat. Commun.*, 2012, **3**, 699.
96 T. Kato and R. Hatakeyama, *Nat. Nanotechnol.*, 2012, **7**, 651–656.
97 M. T. Pettes, H. Ji, R. S. Ruoff and L. Shi, *Nano Lett.*, 2012, **12**, 2959–2964.
98 T. Xia, X. Hu, B. Heng, X. Chen, W. Huang, W. Tao, H. Wang, Y. Tang, X. Tan and X. Huang, *J. Alloys Compd.*, 2013, **549**, 147–151.
99 S.-M. Yoon, W. M. Choi, H. Baik, H.-J. Shin, I. Song, M.-S. Kwon, J. J. Bae, H. Kim, Y. Lee, J.-Y. Lee and J.-Y. Choi, *ACS Nano*, 2012, **6**, 6803–6811.
100 X. Xiao, J. R. Michael, T. Beechem, A. McDonald, M. Rodriguez, M. T. Brumbach, T. N. Lambert, C. M. Washburn, J. Wang, S. M. Brozik, D. R. Wheeler, D. B. Bruckel and R. Polsky, *J. Mater. Chem.*, 2012, **22**, 23749–23754.
101 Z. Yan, Z. Peng, Z. Sun, J. Yao, Z. Liu, P. M. Ajayan and J. M. Tour, *ACS Nano*, 2011, **5**, 8187–8192.
102 Z. Peng, Z. Yan, Z. Sun and J. M. Tour, *ACS Nano*, 2011, **5**, 8241–8247.
103 K. L. Saenger, J. C. Tsang, A. A. Bol, J. O. Chu, A. Grill and C. Lavoie, *Appl. Phys. Lett.*, 2010, **96**, 153105.
104 J. H. Seo, H. W. Lee, J.-K. Kim, D.-G. Kim, J. W. Kang and M.-S. Kang, *Curr. Appl. Phys.*, 2012, **12**, S131–S133.
105 M. Xu, D. Fujita, K. Sagisaka, W. Watanabe and N. Hanagata, *ACS Nano*, 2011, **5**, 1522–1528.
106 L. M. A. Peerdigao, S. N. Sabki, J. M. Garfitt, P. Capiod and P. H. Beton, *J. Phys. Chem. C*, 2011, **115**, 7472–7476.
107 J. M. Garcia, R. He, M. P. Jiang, P. Kim, L. N. Pfeiffer and A. Pinczuk, *Carbon*, 2011, **49**, 1006–1012.
108 R. S. Weatherup, C. Baehtz, B. Dlubak, B. C. Bayer, P. R. Kidambi, R. Blume, R. Schloegl and S. Hofmann, *Nano Lett.*, 2013, **13**, 4624–4631.
109 W. Xiong, Y. S. Zhou, L. J. Jinag, A. sarkar, M. Mahjouri-Samani, Z. q. Xie, Y. Gao, N. J. Lanno, L. Jiang and Y. F. Lu, *Adv. Mater.*, 2013, **25**, 630–634.
110 H.-J. Shin, W. M. Choi, S.-M. Yoon, G. H. Han, Y. S. Woo, E. S. Kim, S. J. Chae, X.-S. Li, A. Benayad, D. D. Loc, F. Gunes, Y. H. Lee and J.-Y. Choi, *Adv. Mater.*, 2011, **23**, 4392–4397.
111 J. T. Smith, A. D. Franklin, D. B. Farmer and C. D. Dimitrakopoulos, *ACS Nano*, 2013, **7**, 3661–3667.
112 J. Lahiri and M. Batzill, *Appl. Phys. Lett.*, 2010, **97**, 023102.
113 W. S. Leong, H. Gong and J. T. L. Thong, *ACS Nano* DOI: 10.1021/nn405834b.
114 L. C. Campos, V. R. Manfrinato, J. D. Sanchez-Yamagishi, J. Kong and P. Jarillo-Herrero, *Nano Lett.*, 2009, **9**, 2600–2604.
115 L. Ci, Z. Xu, L. Wang, W. Gao, F. Ding, K. F. Kelly, B. I. Yakobsen and P. M. Ajayan, *Nano Res.*, 2008, **1**, 116–122.
116 D. Prasai, J. C. Tuberquia, R. R. Harl, G. K. Jennings and K. I. Bolotin, *ACS Nano*, 2012, **6**, 1102–1108.
117 V. R. Galakhov, A. S. Shkvarin, A. S. Semenova, M. A. Uimin, A. A. Mysik, N. N. Shchegoleva, A. Ye. Yermakov and E. Z. Kurmaev, *J. Phys. Chem. C*, 2010, **114**, 22413–22416.
118 P. K. Nayak, C.-J. Hsu, S.-C. Wang, J. C. Sung and J.-L. Huang, *Thin Solid Films*, 2013, **529**, 312–316.
119 Y. S. Dedkov, A. Generalov, E. N. Voloshina and M. Fonin, *Phys. Solid State*, 2011, **5**, 226–228.
120 B. Dlubak, M.-B. Martin, R. S. Weatherup, H. Yang, C. Deranlot, R. Blume, R. Schloegl, A. Fert, A. Anane, S. Hofmann, P. Seneor and J. Robertson, *ACS Nano*, 2012, **6**, 10930–10934.
121 R. Addou, A. Dahal and M. Batzill, *Nat. Nanotechnol.*, 2013, **8**, 41–45.
122 Y. S. Dedkov, M. Fonin, U. Ruediger and C. Laubschat, *Appl. Phys. Lett.*, 2008, **93**, 022509.
123 R. Addou, A. Dahal and M. Batzill, *Surf. Sci.*, 2012, **606**, 1108–1122.
124 O. Vilkov, A. Fedorov, D. Usachov, L. V. Yashina, A. V. Generalov, K. Borygina, N. I. Verbitskiy, A. Grüneis and D. V. Vyalikh, *Sci. Rep.*, 2013, **3**, 168.

